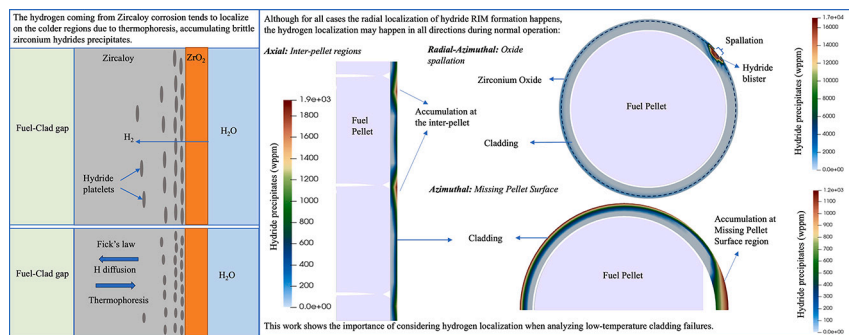


# Modeling hydrogen localization in Zircaloy cladding subjected to temperature gradients

Katheren R.B. Nantes\*, Miaomiao Jin, Arthur T. Motta

Ken and Mary-Alice Lindquist Department of Nuclear Engineering, Pennsylvania State University, Hallowell Bldg., University Park, 16802, PA, USA

## GRAPHICAL ABSTRACT



## ARTICLE INFO

### Keywords:

Hydrogen diffusion  
Hydride localization  
Zircaloy failure  
BISON

## ABSTRACT

In light water reactors, Zr-based alloys used for nuclear fuel cladding undergo oxidation and absorb hydrogen, which can precipitate as brittle zirconium hydrides. During reactor normal operation conditions, hydrogen concentration varies locally due to various factors, where local high concentration can significantly degrade cladding mechanical properties and, hence, its service life. This study aims to quantify the redistribution of hydrogen within the fuel rods caused by temperature gradients, considering geometric irregularities such as inter-pellet regions, oxide spallation, and missing pellet surfaces. Through simulations, we have discovered that these temperature variations can lead to significant local hydrogen enrichment, even under normal operational conditions. Consequently, the Zircaloy cladding may suffer from critical weakening in its mechanical performance due to excessive hydride precipitation at specific locations. These findings underscore the importance of accounting for local hydrogen concentrations when evaluating the overall reliability of the cladding.

## 1. Introduction

In light water reactors, Zr-based alloys are typically used as nuclear fuel cladding [1], which is oxidized during service by the cooling water, and the corrosion reaction generates hydrogen, some of which

is absorbed into the cladding through a process known as hydrogen pickup [2–4]. At a certain temperature, when the cladding concentration of hydrogen in solution exceeds its Terminal Solid Solubility for precipitation (TSSp), it can form hydride precipitates, and when the concentration at a temperature reaches the Terminal Solid Solubility

\* Corresponding author.

E-mail address: [krm5198@psu.edu](mailto:krm5198@psu.edu) (K.R.B. Nantes).

<https://doi.org/10.1016/j.jnucmat.2023.154853>

Received 21 August 2023; Received in revised form 27 November 2023; Accepted 30 November 2023

Available online 6 December 2023

0022-3115/© 2023 Elsevier B.V. All rights reserved.

for dissolution (TSSd), the hydride platelets start dissolving [5–8]. As at the reactor operating temperature, the hydrogen that is picked up can redistribute within the cladding tube, driven by concentration, temperature, and stress gradients, potentially creating high local hydrogen concentrations [5]. Such local hydrogen concentrations then control the overall cladding ductility and indeed the cladding life, because of the brittle hydride particles that severely degrade the cladding's ductility.

There are three factors that determine the hydrogen flux. First, the hydrogen concentration gradients follow Fick's law of diffusion. Second, in the nuclear fuel rods during operation, a temperature gradient is established between the inner and outer cladding surfaces, and the Soret effect (also known as thermophoresis) leads to hydrogen flux from the hot to the cold parts of the sample. Lastly, any gradient in hydrostatic stress also influences the migration of hydrogen. Combining these three hydrogen migration driving forces, the overall hydrogen flux is given by:

$$J_H = -D_H \nabla C_{ss} - D_H \frac{Q^* C_{ss}}{RT^2} \nabla T + D_H \frac{C_{ss}}{RT} \nabla \sigma_H, \quad (1)$$

where  $D_H$  is the diffusion coefficient of hydrogen in Zr,  $C_{ss}$  is the concentration of hydrogen in solid solution,  $Q^*$  is the heat of transport of hydrogen in Zr,  $T$  is the temperature,  $R$  is the ideal gas constant,  $V$  is the molar volume of hydrogen in Zr, and is the hydrostatic stress gradient. For our case of interest, the diffusion along hydrostatic stress gradients is assumed to be negligible compared to the other contributions at the engineering scale and will not be accounted for in this study. The assumption is supported by calculations in Appendix A.

While the hydrogen flux resulting from Fick's law of diffusion tends to homogenize the hydrogen in solution concentration, the hydrogen flux due to the Soret effect tends to concentrate hydrogen in solution in the colder parts of the cladding tube. This means that, hydrogen in solution tends to accumulate in the colder spots, which can give rise to the formation of zirconium hydrides, impacting the mechanical performance of the cladding at those spots. Several examples exist in the literature where temperature gradients drive the redistribution of hydrogen in solution in Zr alloy fuel rods due to structural irregularities, as discussed in Section 4. This redistribution can happen in the three tube directions, i.e., axial, radial, and azimuthal directions, which are exemplified in the three scenarios: pellet stacking, oxide spallation, and missing pellet surface (MPS), respectively. Due to the coupling between hydrogen transport, hydrogen precipitation, and heat transport, it is not feasible to provide an analytical solution. In this work, we numerically solve, for those three scenarios, the coupled partial differential equations for heat conduction, stress-strain deformation, Zircaloy oxidation, hydrogen in solid solution transport and zirconium hydride precipitation, using the Finite Element Method code BISON [9], to demonstrate that during normal reactor operation, it is possible to establish temperature gradients (radially, axially and azimuthally) that lead to strong enrichment of hydrogen at specific locations, which can cause excessive hydride precipitation. The findings of our calculations are subsequently discussed in light of existing observations in the literature. By shedding light on these hydrogen concentration variations and their consequences, this study contributes to a better understanding of cladding behavior under normal operational conditions.

## 2. Methods

Among the modeling that exists in literature, we can note the work of Asher and Trowser [10] which proposed that the hydrogen terminal solid solubility should be described by a noisy curve, as the hydride platelets can be precipitated in different phases and in preferential planes and lattice sites. We also note the work of Marino [11,12], who also proposed a method to model hydrogen precipitation assuming a precipitation rate proportional to the hydrogen supersaturation in the material, which was further studied by Lacroix et al. [8] and found not to accurately describe the hydride precipitation. Therefore, for the

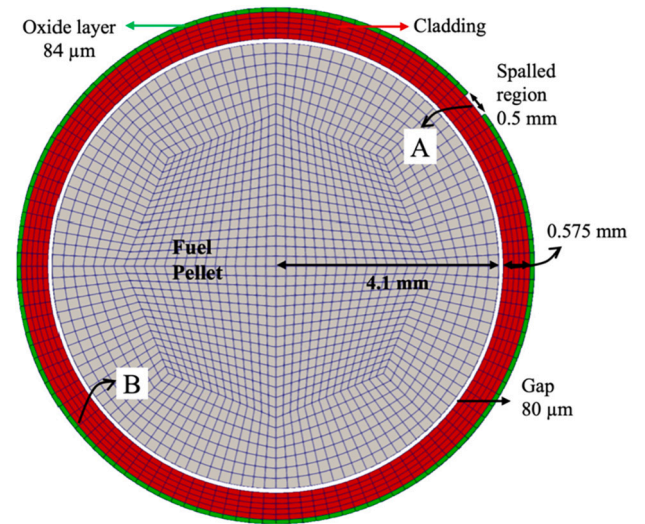


**Fig. 1.** Geometry and meshing of a rod cross-section with a 0.5 mm wide oxide spalled region. (A) is the blister center and (B) is the symmetric position with respect to the center. (For interpretation of the colors in the figure(s), the reader is referred to the web version of this article.)

simulations of our interest, we have used the modeling available in the nuclear fuel performance code BISON [9], which is based on the MOOSE framework [13], to solve three coupled physics problems for heat transfer, deformation, and hydrogen transport and precipitation using a typical fuel rod geometry, transient type and Preconditioned Jacobian-Free Newton Krylov solver type [13]. To understand local hydrogen accumulation under normal operation conditions, three sets of simulations are performed including, (i) inter-pellet accumulation of hydrogen, in axisymmetric R-Z coordinates, (ii) oxide spallation, and (iii) MPS, in R- $\theta$  coordinates. In each case, both the temperature and hydrogen distributions are calculated, and the hydride concentration is used to evaluate its potential to create weak spots.

For the simulation of inter-pellet accumulation of hydrogen, the rodlet is simulated up to 63 GWd/tU using the parameters for the REP-Na10 [14] experiment, to be described in the Results section. To solve the temperature distribution, a heat source is imposed on the fuel via the cosine power profile. For simplicity, fragmentation of the fuel pellets is not considered, although it should be noted that it may lead to even greater hydrogen localization. Thermal contact is modeled by a gas gap model, which estimates the gap conductivity and pressure based on the amount of fission gas released [9,15]. The fuel and cladding thermal conductivities are estimated based on MATPRO equations [16]. The pellet-cladding contact is assumed frictional with a friction coefficient of 0.65 [17]. Furthermore, a penalty function is introduced to prevent the nonphysical overlap of fuel and cladding mesh surfaces during mechanical contact [18]. To obtain the hydrogen distribution, the HNGD model of hydrogen in solution migration and hydride precipitation, growth and dissolution [6,7] is used in BISON, the details of this model can be found in Appendix B. This model combined with the Zircaloy oxidation [19] at normal operation temperature, EPRI KWU CE Model, and hydrogen pickup models, using a constant hydrogen pickup fraction of 20% can enable a description of hydrogen distribution as a function of burnup. For the deformation, we consider irradiation swelling and thermal expansion of the cladding, irradiation creep and growth of the cladding, and irradiation swelling and thermal expansion of the fuel pellet. In the cladding, the empirical Limback-Hoppe creep model is used, which applies the Limback-Andersson correlation for primary and secondary thermal creep [20], and the Hoppe correlation for irradiation creep [21] on the Zircaloy-4 cladding. More information on each model can be found in [22–24].

To investigate the effects of oxide spallation, mesh shown in Fig. 1 and MPS, mesh shown in Fig. 2, we examine the cross-section of a fuel

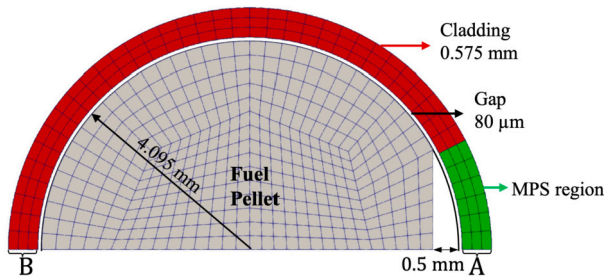


Fig. 2. Missing Pellet Surface model mesh.

rod using simplified models. These models include constant heat generation within the fuel, a constant gap conductivity of 5500 W/mK, and an initial hydrogen concentration distributed uniformly throughout the material. The primary objective of these simulations is to observe how the hydrogen already within the material reacts to the sudden occurrence of oxide spallation or the presence of MPS. We note that the assumption of uniform distribution of hydrogen is not realistic, as in normal operation conditions hydrogen would naturally redistribute. We also note that a sudden onset of MPS is not physically realistic, as it is believed to be a fabrication defect. However, the purpose of this study is to understand how the MPS configuration or the occurrence of oxide spalling can create a temperature gradient that causes hydrogen to redistribute as hydrogen is present in the cladding. By examining these scenarios, we aim to gain insights into the behavior of the material and the hydrogen redistribution under such conditions.

### 3. Results

#### 3.1. Hydrogen accumulation in the inter-pellet region

We utilize the parameters for the rodlet based on the REP-Na10 experiment [14], one of the experiments conducted at the CABRI facility in Cadarache, France, to test the susceptibility of irradiated hydrided cladding to a reactivity-initiated accident (RIA). The parameters are summarized in Table 1.

In this simulation, a rodlet of approximately 59 cm in height was used, with fuel at a burnup of 63 GWd/tU. Our current analysis is performed at a burnup of 54 GWd/tU to represent a high burnup condition. The linear power history for the irradiation of this rodlet is based on the data provided in [27] and is shown in Fig. 3. At the specified burnup, the calculated oxide thickness was approximately 64 microns near the center of the rodlet, which corresponds to an average hydrogen concentration of 474 wppm.

Due to the lower heat flux at the inter-pellet location compared to the mid-pellet location, the temperature in these regions remains correspondingly lower throughout the irradiation time. Consequently, the Soret effect drives the accumulation of hydrogen in these lower-temperature regions. Fig. 4a depicts the axial temperature ( $T$ ) distribution as a function of rodlet height for REP-Na10 at 54 GWd/tU, while Fig. 4b shows the corresponding total hydrogen concentration ( $C_H$ ), at both the inner and outer cladding surfaces. From the peak locations, it can be seen that the significant difference in hydrogen concentration between the inner and outer cladding is correlated with the radial temperature gradient. Fig. 4c shows the correlation between total hydrogen content and temperature at each node of inner and outer cladding, so it illustrates the correlation between temperature and hydrogen content. It can be seen that high temperature at the inner cladding surface leads to low hydrogen content, while at the outer surface, a certain temperature can exhibit a broad range of hydrogen concentrations, as a result of coupling with the local gradient of temperature, signifying the importance of temperature gradients inducing strongly-enriched hydrogen regions.

The orange line in Fig. 4b represents the average hydrogen concentration in the cladding at 474 wppm. Upon examining this hydrogen dis-

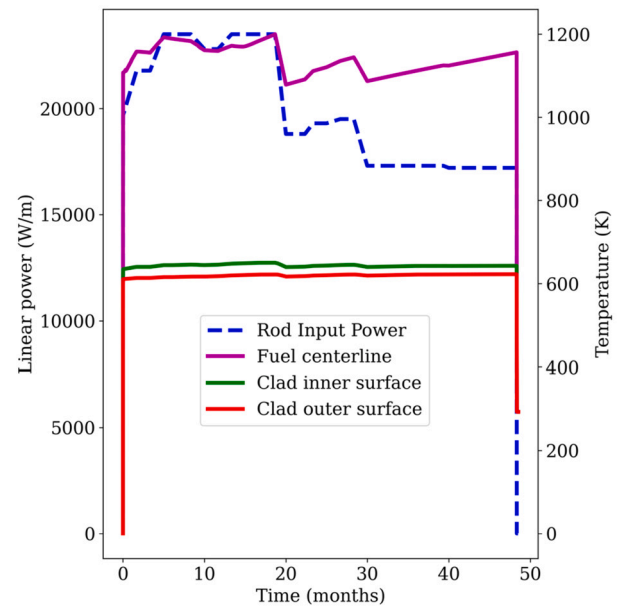


Fig. 3. Linear power history used for simulating the rodlet irradiation up to 63 GWd/tU burnup, and the fuel centerline temperature, cladding inner and outer wall average temperatures.

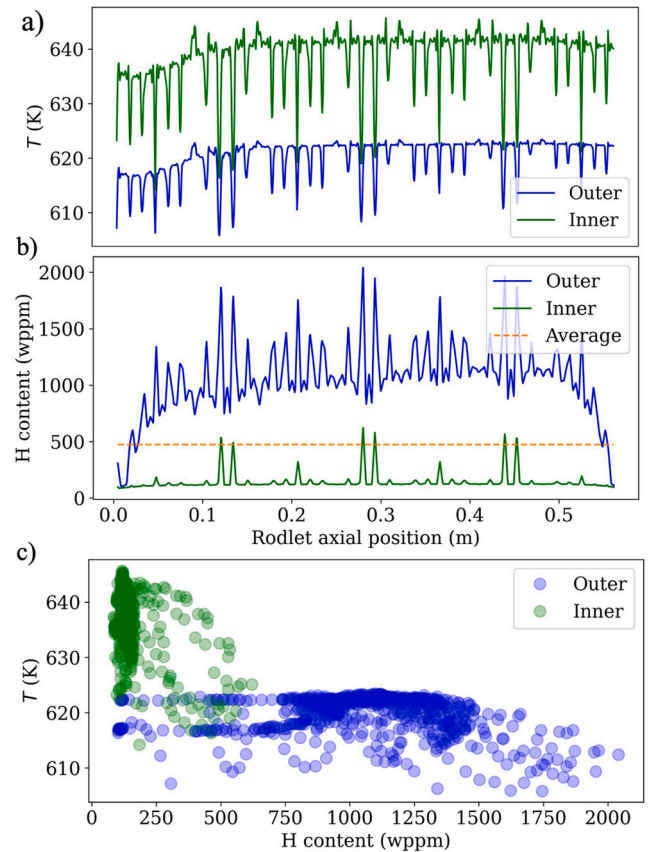


Fig. 4. As part of this work simulation results, at fuel burnup of 54 GWd/tU, 40 months of irradiation: a) Cladding temperature distribution and b) Total hydrogen content (hydrogen in solution + hydrogen precipitated) distribution, where the blue curve represents the outer cladding, the green curve represents the inner cladding, and the orange line represents the cladding average. c) Temperature and hydrogen content correlation at outer cladding (blue) and inner cladding (green).



**Table 1**  
CABRI REP-Na10 rodlet simulation parameters.

Fuel type	UO <sub>2</sub>
Cladding type	Zircaloy-4
Initial enrichment	4.5 ( <sup>235</sup> U/U %)
Internal gas pressure	0.301 MPa
Initial Plenum Gas type	He
Number of Fuel Pellets	39
Fuel Pellet height	14.25 mm
Active length	559 mm
Maximum burnup	63 GWd/tU
Average corrosion thickness	80 μm
Cladding outer diameter	9.51 mm
Cladding thickness	0.575 mm
Fuel Pellet diameter	8.19 mm
Fuel-cladding gap	82 μm
Fuel-cladding top gap	0.032 m
Fuel-cladding bottom gap	0.003 m
Top and bottom clad thickness	0.0015 m
Chamfer height	0.5 mm
Chamfer width	0.55 mm
Dish depth	0.205 mm
Dish radius	3 mm
Normal operation inlet Coolant Temperature	588.7 K
Initial Coolant Heat Transfer Coefficient	34,535 W/m <sup>2</sup> K
Fuel emissivity	0.798 [25]
Cladding emissivity	0.325 [26]

tribution along the axial direction, we note that the peaks in hydrogen concentration roughly align with the inter-pellet regions. Another point needs to be made concerning the variation in hydrogen peak heights seen in Fig. 4b. The three pairs of high hydrogen locations at 0.11–0.12, 0.28–0.29, and 0.43–0.44 m are caused by numerical variations, likely an artifact of the pellet-cladding contact model used in BISON. Regardless of this numerical issue, it is clear that the pellet-pellet interfaces lead to hydrogen concentrations that are considerably higher than the average concentration. This means that these high hydrogen concentration regions would be where failure likely occurs in case the whole cladding is strained. Overall, the figure illustrates that most points on the cladding outer surface lie above the average line. This observation suggests that relying solely on the average hydrogen concentration in the cladding may not be an effective predictor of cladding failure. The reason for this lies in the fact that the cladding tends to fail at its weakest point, which often corresponds to a location with a high hydrogen concentration. Such high concentrations can lead to the formation of local hydrides, consequently weakening the material through embrittlement. Therefore, it is crucial to consider the spatial distribution of hydrogen concentration, as opposed to relying solely on the overall average concentration to gain a more accurate understanding of potential cladding failure under stress.

For a closer examination, Fig. 5 shows contour plots of (a) the temperature distribution and (b) hydrogen as hydride concentration in the cladding near a fuel pellet at a height of 0.29 m from the bottom of the rodlet. It reveals a temperature difference of approximately 10 K between the mid-pellet and the inter-pellet region, marked by the black dots. As discussed above, this drives the concentration of hydrogen precipitated as hydrides ( $C_p$ ) to be much higher at the inter-pellet cladding location than at the mid-pellet cladding location, which yields a difference of 883 wppm. For a better comparison and interpretation, Fig. 6a shows the radial temperature gradient along the cladding thickness at the mid-pellet and inter-pellet height, and Fig. 6b shows the radial distribution of hydride precipitates concentration along the same region.

**Table 2**  
Oxide spallation model setup.

Fuel type	UO <sub>2</sub>
Cladding type	Zircaloy-4
Cladding outer diameter	9.51 mm
Cladding thickness	0.575 mm
Fuel Pellet diameter	8.19 mm
Fuel-cladding gap	80 μm
Oxide Thickness	84 μm
Spallation size	0.5 mm
Linear Power	19.6 kW/m
Coolant bulk temperature	592 K

### 3.2. Hydrogen redistribution upon oxide spallation

When the oxide layer reaches a certain thickness, typically around 80 microns, portions of the oxide can spall off [28]. This oxide spallation creates a thinner oxide region, thereby reducing the heat transfer resistance of the cladding to the coolant, and causing the local cladding temperature to decrease. Such temperature decreases can be quite significant, and cause the hydrogen to flow from the hotter regions in the cladding to the region near the spalled oxide, thus creating a hydride blister as has been observed in [29]. Such blisters can be quite deep, reaching over 50% of cladding thickness [30]. When the cladding is subjected to hoop strain, as can happen due to pellet cladding mechanical interaction, the brittle blister is prone to crack at low strain levels. This crack localizes any further deformation to the region underneath the blister, consequently reducing the overall failure strain.

To the best of our knowledge, there are no established models to predict oxide spalling. Hence, in our simulation, it is assumed that a portion of the oxide spalls at time zero. Subsequently, we investigate the evolution of hydrogen distribution in response to this spalling event. As a first approximation, although the spalled oxide is realistically a three-dimensional spot, the simulation is conducted in two dimensions ( $r$ - $\theta$ ). The starting oxide thickness is assumed to be 84 microns. Based on the corrosion model for Zircaloy-4 [19], and assuming a 20% hydrogen pickup fraction, this corresponds to an average hydrogen concentration of 700 wppm. Initially, the hydrogen is assumed homogeneously distributed in the cladding. Given the high concentration, a large fraction of the hydrogen would be in the form of homogeneously distributed hydride particles. Although the hydrogen pickup could increase at the spalled region, in the short time of this simulation very little pickup is expected to occur, so this is not modeled here. The simulation utilizes a linear power of 19.6 kW/m in the fuel, a 0.5 mm spalled oxide region, and the bulk coolant temperature is fixed at 592 K. All simulation input data can be found in Table 2.

The temperature distribution and hydrogen concentration in the cladding approach quasi-steady state after roughly 10 days, in this case, we assess a steady state by a diminishing percentage change of hydrogen content at the blister center, compared with the initial concentration. We deem a steady state to have been achieved when this change is stable, as shown in Fig. 7, the negative percentage represents when the hydrogen precipitates and the positive changes represent the hydrogen migration, one can see that after around 10 days there are no strong variations compared to the first 5 days. At 10-day timestep, the  $T$  and  $C_p$  distribution in the ( $r$ - $\theta$ ) region are shown in Fig. 8 (a-b). To reveal the impact of the oxide spallation, both variables are plotted along the dashed symmetry line (Fig. 8 (c-d)), to show the difference from points (A) and (B) in Fig. 1, and along the azimuthal direction at metal-oxide interface surface (Fig. 8 (e-f)). From the temperature distribution, it can be seen that the oxide layer largely reduces the cladding temperature, and there is a temperature difference of 33 K, measured from an average taken around the center of the spalled region to an average taken around a corresponding point 180 degrees away in the cladding

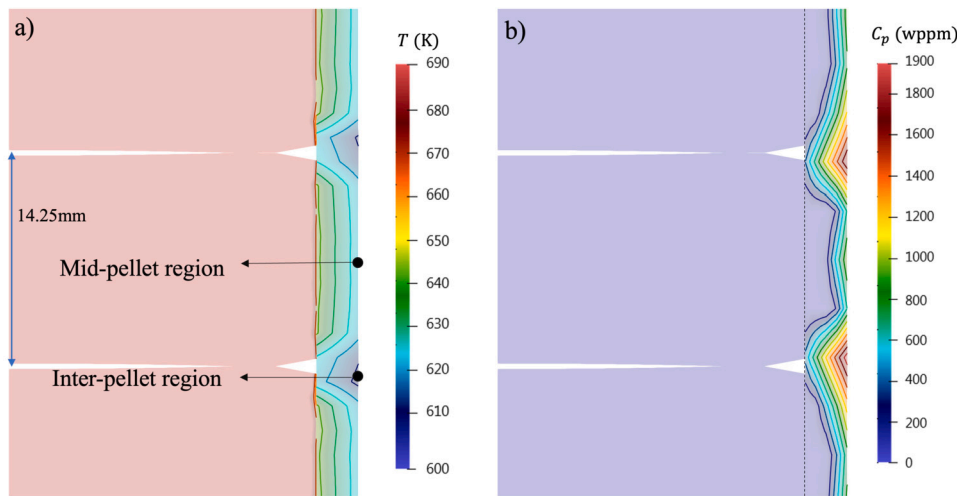


**Fig. 5.** Contour plots for (a) temperature distribution and (b) hydride concentration at the rodlet center height, at 0.29 m from the bottom of the pin. These distributions are shown at a fuel average burnup of 54 GWd/tU and average hydrogen in hydride concentration of 474 wppm. (Figures scaled 5x in the radial direction).

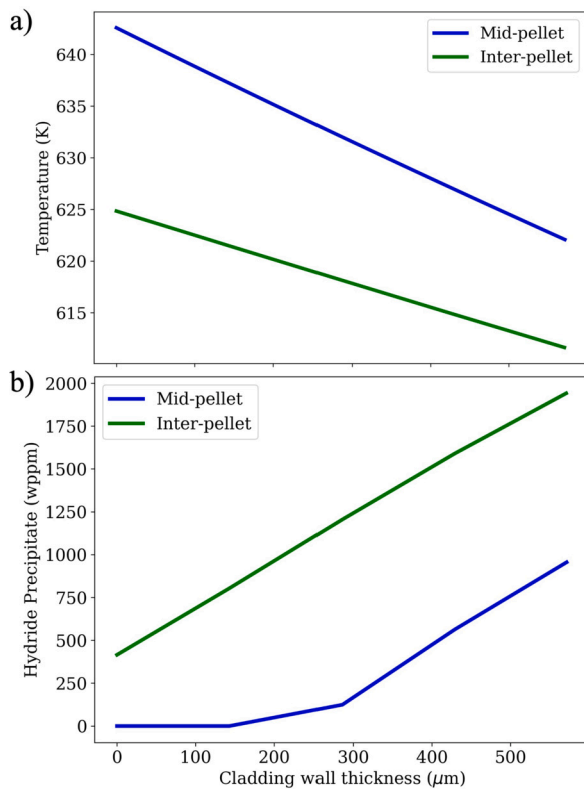


**Fig. 6.** Radial profile of (a) temperature and (b) hydrogen precipitates concentration at the mid-pellet and inter-pellet regions, for a correspondent burnup of 54 GWd/tU, or after 40 months of irradiation.

(points A and B, respectively, on Fig. 1). Given this temperature gradient and the high mobility of hydrogen in zirconium, a quasi-steady state of hydrogen distribution is achieved in 10 days. This suggests that hydrogen accumulation near the spalled region occurs relatively quickly compared to the overall operation time.

From Fig. 8b and 8d, it can be seen that the local hydrogen concentration can increase significantly ( $> 15,000$  wppm), much higher than that without oxide spallation. Consistent with experiments, to be discussed in Section 4, hydride blisters near the spalled oxide location have been reported in the literature [30], indicating the very high  $C_p$  at the spalled region.

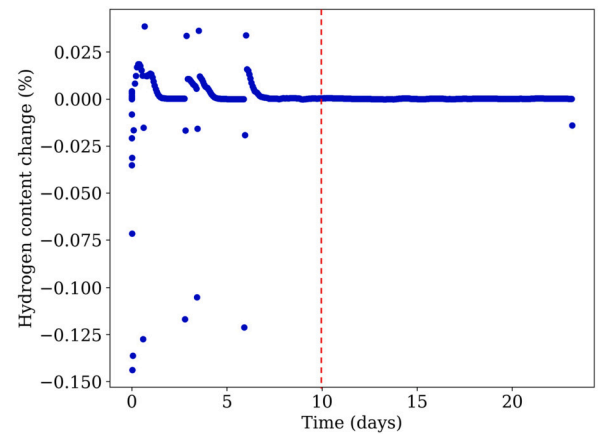


**Fig. 7.** Percentage of change in hydrogen content ( $C_h$ ) with time, measured at the blister outer surface center node.

### 3.3. Missing pellet surface

The final case we simulate is that in which a fuel pellet is fabricated with an MPS, leading to an inhomogeneity in the temperature distribution and the hydrogen distribution. The simulation model and meshing are shown in Fig. 2 with parameters listed in Table 3. The hydrogen concentration is assumed to be initially homogeneous and equal to 400 wppm. For simplicity, we assume there is no oxide present, as the uniform oxide layer on the cladding surface is believed to have minimal effect on how the homogeneous hydrogen distribution would redistribute itself due to the presence of MPS.

With MPS, a quasi-steady state is established in approximately 6 days, which is determined similar to the oxide spallation model, by the percentage change in average hydrogen concentration at region A of Fig. 2. In Fig. 9, the percentage change starts highly negative due to precipitation of the excess of hydrogen in solid solution to hydrides, as 400 wppm seems to be a high concentration for the starting temperature, and then this percentage starts increasing due to the hydrogen diffusion to the MPS region and decreases once again due to further hydride formation. Accordingly, the steady-state time was chosen as 6 days, when the percentage change is around 0.02%. At quasi-steady state, Figs. 10 (a-b) show the contour plots of temperature and hydride concentration, respectively. Although MPS creates an increased gap (thermal resistance), it also reduces the effective heat flux from

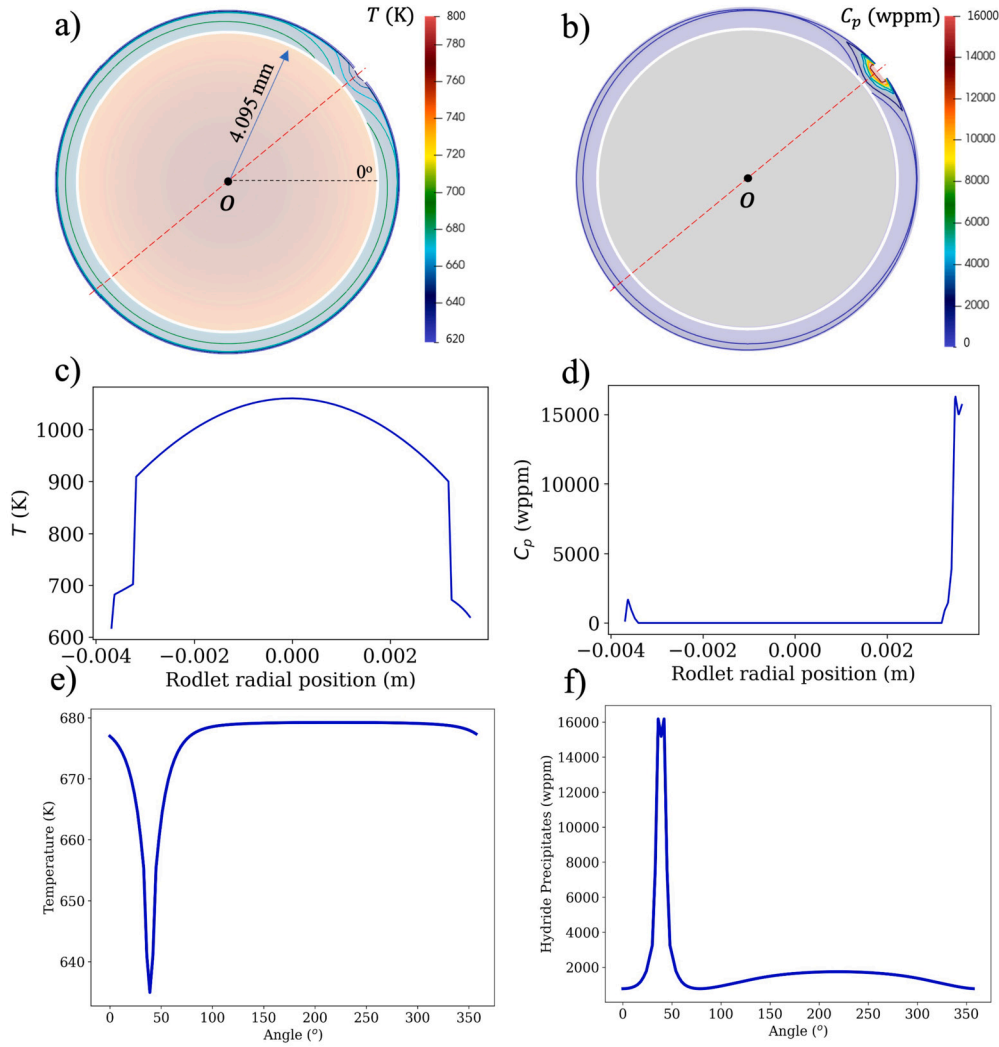


**Fig. 8.** At 10 days after the oxide is spalled: a) Temperature contour plot; b) Contour plot of the concentration of hydrogen precipitated as hydrides; Correspondingly, (c-d) shows the profiles at the symmetry line (red dashed line), and (e-f) show the azimuthal distribution of temperature and hydride precipitates concentration, respectively. The angle is measured starting from the black dashed line counter-clockwise.

**Table 3**  
Missing pellet surface model setup.

Fuel type	UO <sub>2</sub>
Cladding type	Zircaloy-4
Cladding outer diameter	9.51 mm
Cladding thickness	0.575 mm
Fuel Pellet diameter	8.19 mm
Fuel-cladding gap	80 $\mu$ m
MPS depth	0.0005 m
Linear Power	19.3 kW/m
Coolant bulk temperature	588.70 K

fuel to cladding, resulting in a local lower cladding temperature. From Fig. 10c, which illustrates the temperature profile along the symmetry line, a temperature difference of 22 K is identified via  $T_B - T_A$ , where  $T_A$  and  $T_B$  are the average temperature values at A and B regions indicated in Fig. 2, respectively. Furthermore, it can be seen that within 6 days, the cladding near the MPS region can be significantly enriched with hydrides compared to the region without MPS (Fig. 10b). From the hydrogen profile in Fig. 10d, hydride precipitation occurs all across the coolant side of the cladding, but becomes more spread near the MPS region, leading to a higher average hydride concentration. For

better visualization, Fig. 11 shows the temperature and hydride precipitate concentration along the azimuth direction, at the inner and outer cladding radius. The hydride concentration at the outer cladding for the region next to the missing pellet surface and to the opposite direction is the same because the hydride precipitation would have reached the limit. The sudden decrease in the outer clad hydride concentration is due to hydrogen migration from that region to the MPS region. Therefore, the most important point to note is the much higher concentration at the inner cladding next to the missing pellet surface than on the opposite side.

A summary of the results presented is shown in Table 4, where  $C_h^{Avg}$  represents the total cladding hydrogen average, and  $t_{ss}$  represents the time considered to reach steady state. In each case the  $\Delta T$  and  $\Delta C_h$  values are calculated by comparing the difference in temperature and average hydrogen concentration ( $C_{ss} + C_p$ ) between (i) the mid-pellet and inter-pellet locations, (ii) the middle of the spalled oxide location and the corresponding cladding location 180 degrees away and (iii) the middle of the MPS region and the corresponding location 180° away. Significant hydrogen accumulations at the relatively colder spots can occur in each case. Because the configurations and the temperature gradients differ from case to case, the values are not directly comparable to establish a positive correlation between  $\Delta T$  and  $\Delta C_h$ . These scenarios demonstrate that the temperature differences that can be expected during normal operation can significantly change the

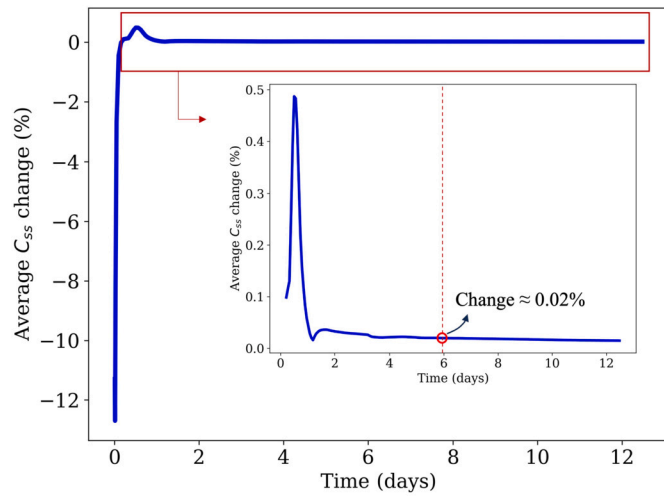


**Fig. 9.** Evolution of the percentage change in average hydrogen in solid solution in the cladding MPS region, indicated in Fig. 2. The inner plot is a zoom into the original plot after all initial excess hydrogen has already precipitated. The red dashed line represents the time considered as steady-state.

**Table 4**

Analysis data summary.

Case	$\Delta C_h$ (wppm)	$\Delta T$ (K)	$C_h^{Avg}$ (wppm)	$t_{ss}$
Inter-pellet	883	12	474	n/a
Oxide Spall	7335	33	755	10 days
MPS	586	22	453	6 days

local hydrogen concentrations, which ultimately controls cladding failure. Hence, the average hydrogen concentration in the cladding is likely not the most accurate measure of cladding embrittlement, as commonly used in previous determination of Zr cladding failure limits due to hydrogen embrittlement [31].

#### 4. Discussion

It is important to emphasize that hydrogen redistribution is not contingent on the degree of oxidation at a particular cladding location; rather, it relies on the existing hydrogen within the material migrating to regions with lower temperatures. The driving force behind this migration is the Soret effect, leading to preferential precipitation of hydride in these colder areas due to the lower hydrogen solubility at such locations.

The most often reported observation is the formation of a hydride rim when the cladding is hydrided in service [32]. The low outer cladding temperature causes hydrogen to migrate there from the inner cladding. This low-temperature region is also associated with the lowest hydrogen terminal solid solubility in the cladding. Both these effects cause hydride rims to form near the outer cladding surface, the hydrogen concentration of which is approximately 2,000–3,000 wppm [33], and which grow in thickness with increased reactor exposure. When subjected to a hoop strain such as would occur from pellet-cladding mechanical interaction (PCMI), such hydride rims will crack at a small strain, thus localizing further deformation and embrittling the material by causing the overall failure strain of the cladding to decrease [14,32]. Fig. 12 (a) shows a hydride rim formed on a Zircaloy-4 fuel rod [32].

Due to the stacking of fuel pellets in fuel rods, along the axial direction, it is well known that the inter-pellet region is associated with lower cladding temperature and is thus susceptible to hydrogen accumulation [29], which is also confirmed by the current calculations (Fig. 5). Fig. 12b, reproduced from reference [29] shows significantly

**Table 5**

Average hydrogen concentrations (wppm) at the indicated azimuth locations for the five rods examined in [39], including Gravelines GAI, Gravelines GAAI, Fessenheim FAI, Fessenheim FAAI, and Cruas.

Azimuth	Gravelines GAI	Gravelines GAAI	Fessenheim FAI	Fessenheim FAAI	Cruas
0	374	305	244	301	154
90	419	420	219	298	271
180	415	264	218	287	198
270	379	367	350	342	159
$\beta$	0.12	0.46	0.51	0.18	0.60

higher hydride concentration at the cladding location near the pellet interface than at the mid-pellet location.

It is also possible that the temperature is lowered in a localized region. A classic example is the formation of hydride blisters underneath a region of spalled oxide. The growing  $ZrO_2$  oxide layer formed by waterside corrosion represents a resistance to the heat flux from the fuel rod to the coolant, which causes the cladding temperature to rise during service. As aforementioned, when the oxide layer reaches a thickness of about 80 microns, oxide spallation is possible [28], causing the temperature in the cladding region under the spalled oxide to decrease. Based on our calculation, a temperature difference of 33 K can be established, driving the hydrogen to concentrate at that location. This phenomenon causes the formation of a hydride blister [29], similar to that shown in Fig. 12c. In this case, the spalled region is two dimensional and thus the blister is normally lens-shaped. The hydride blister is often a solid hydride with a hydrogen concentration above 16,000 wppm, which is consistent with our calculations (Fig. 8). The blister depth can span a large percentage of the cladding thickness. Such hydride blisters, seen frequently in rods that have seen severe duty and thus have thick oxide layers and high hydrogen pickup, can significantly decrease cladding ductility [36,37,30].

In the variations with azimuthal dependence (as exemplified in our MPS calculations), we can identify only a few examinations of the hydrogen azimuthal distribution. The work of Lanning and co-workers shows some evidence of this effect [38]. They studied the azimuthal hydrogen distribution in the pressure tubes of the N-reactor after long exposures and found significant hydrogen concentration differences along the azimuth, which they attribute to the temperature gradients present in service. They estimate that an azimuthal temperature difference of approximately 17 K was present in service to be enough to create the observed inhomogeneity in hydrogen distribution. This temperature difference from their estimation is similar to the calculations performed in this study for the MPS case. Fig. 13 (taken from ref. [38]) shows the measured hydrogen concentration along the azimuth for three different tubes in their study, with very high variability in hydrogen concentration along the azimuth.

Other evidence of azimuthal hydrogen re-distribution comes from the work of Zhang [39,40]. In that study, the authors examined irradiated rods from the Fessenheim, Cruas, and Gravelines reactors. These fuel rods were irradiated respectively to burnups of 55.645, 39.635, and 58.230 GWd/tU, and were clad in Zircaloy-4. In each case, the authors took samples from four quadrants (0, 90, 180, and 270°), with four sections in the radial direction of the cladding, so they could study hydrogen distribution in both radial and azimuthal directions. Taking the average radial hydrogen concentration for each quadrant, we obtain the results shown in Table 5.

In the absence of oxide spallation, the possibility of azimuthal temperature gradients depends on the existence of an inhomogeneous heat generation or heat transfer in the nearest neighborhood of the rod during service, although the records of the specific configuration for each rod were not kept. Nevertheless, one can see that there is considerable variation in hydrogen content along the azimuth in three of the five rods. We estimate this variability by calculating for each tube the



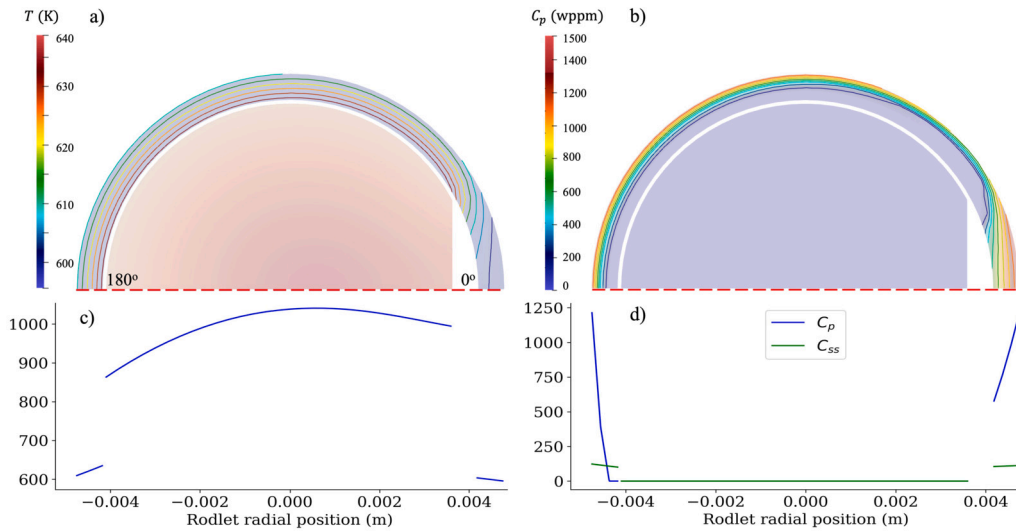


**Fig. 10.** Quasi-steady state results for (a) temperature distribution and (b) precipitated hydrogen content distribution contour plot for MPS case. Correspondingly, (c-d) shows the profiles along the symmetry line (red dashed line) of hydrogen in the form of hydrides ( $C_p$ ) and in solid solution ( $C_{ss}$ ).

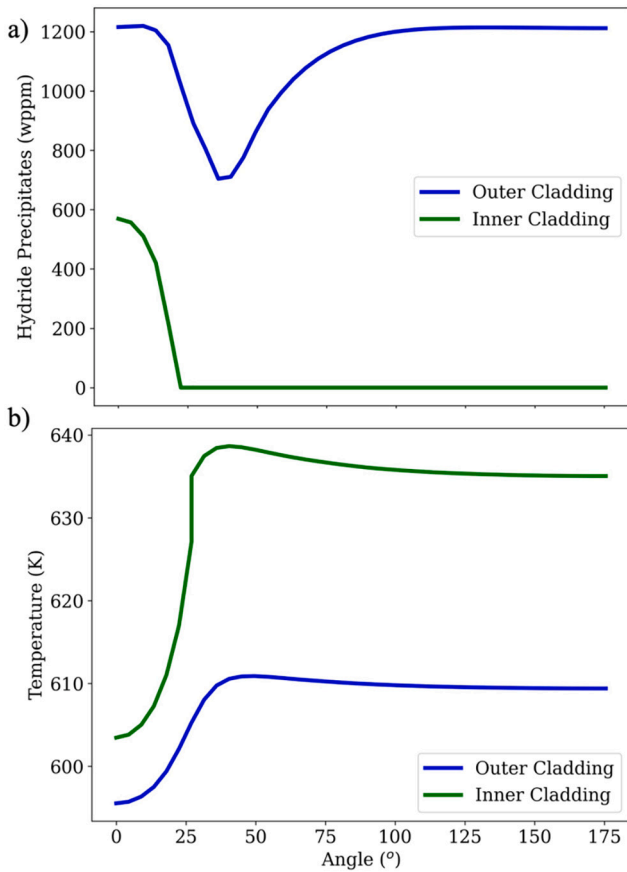


**Fig. 11.** Azimuthal distribution of (a) precipitated hydrides and (b) temperature at the inner and outer cladding for a Missing Pellet Surface event. Where the angle  $0^\circ$  is at the right side of the symmetry line in Fig. 10.

parameter  $\beta = (H_{max} - H_{min})/\bar{H}$ , where  $H_{max}$  and  $H_{min}$  are the maximum and minimum hydrogen concentrations in a given cladding tube and  $\bar{H}$  is the overall average in each case. The largest variation in  $\beta$  was seen in the Cruas rod, with  $\beta = 0.60$ , which means that the variation in hydrogen content from the maximum to the minimum is 60% of the average for the four quadrants, representing a significant change. It is worth noting that every quadrant of all five rods shows a radial

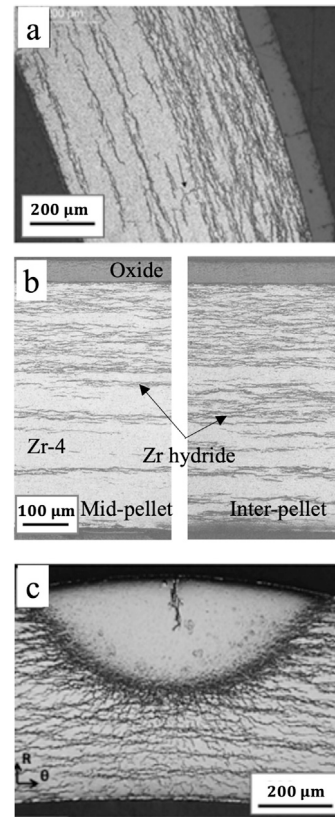


**Fig. 12.** Scanning electron microscope (SEM) images of (a) hydride rim [34], (b) hydride morphology in Zircaloy-4 at the mid-pellet location and at the inter-pellet location [29], and (c) SEM of hydride blister [35].

hydrogen concentration gradient with the highest values being on the outer surface, consistent with our understanding and simulation results.

Finally, recent extensive irradiated rod examinations conducted at Oak Ridge National Laboratory [41] and Pacific Northwest National Laboratory [42] in which the hydrogen content of different rod quadrants were examined showed additional evidence of hydrogen accumulation. For example, out of 13 rods whose hydrogen concentration by quadrant was examined (see Table B-7 of [42]), 6 rods showed values of the  $\beta$  parameter from 0.6 to 0.95; the difference was greater in



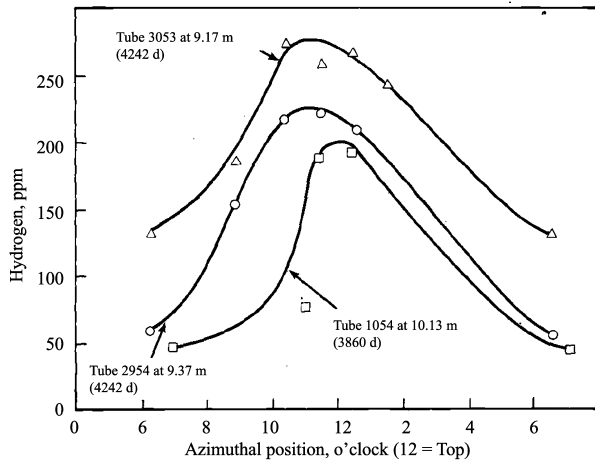


Fig. 13. Azimuthal distribution of hydrogen in N-reactor pressure tubes (numbers in parentheses are the days of operating service for each tube). Adapted from [38].

Zircaloy-4 rods than in M5 or ZIRLO rods. For the later study, evidence was seen of wide hydrogen variation (50 to 100%) along the azimuth in all three cladding types, which may be partly due to oxide spallation [42].

In summary, there is considerable experimental evidence for hydrogen accumulation at cold spots in the cladding during service, which is now supported by the calculations presented in this work. Such hydride accumulations would be susceptible to the sudden hoop strain produced by the pellet swelling and PCMI produced during an RIA, as failure in such a case would occur at the weakest cladding spot, which is the location with the highest hydride content.

In that context, the results of some of the RIA tests previously performed could be re-evaluated, considering the possibility of hydrogen redistribution in service leading to hydride accumulation and the creation of a highly hydrided weak spot which causes failure at small strains. In particular, the very low energy failure observed in the CABRI rod REP-Na1 [43,44] could have occurred because of hydride accumulation. Previous work had concentrated on possible rod re-fabrication defects as a possible explanation for the very low energy failure observed in that test [45]. However, such a hypothesis may not be needed to rationalize the low energy failure observed, as the fuel rod in question was irradiated to 67 GWd/tU, had a very thick oxide layer (average of 90 microns), had an overall hydrogen content of ~700 wppm and showed extensive oxide spallation. In such a condition, one could expect that hydride blisters would form and would severely embrittle the cladding, causing it to fail at very low deposited energy.

Those results show how important it is to consider the hydrogen localization when analyzing a Zircaloy cladding failure. In the case of simulating cladding failure induced by zirconium hydride embrittlement, the current criteria in fuel performance modeling [31] use only total cladding average hydrogen concentration, and therefore, do not yet take into account the possibility of hydrogen localization during service driven by temperature gradients.

## 5. Conclusions

This study presented three models to analyze the variations in local hydrogen concentration caused by three types of temperature inhomogeneities, that could be present during normal reactor operation: the inter-pellet region, oxide spallation, and missing pellet surface. The conclusions are:

1. Hydrogen migration in zirconium is fast enough that compared to the rod irradiation time hydrogen can respond relatively quickly

to create a new hydrogen distribution with significant variations in hydride concentration along the three tube directions.

2. Significant hydrogen accumulations are observed in all these cases such that the local hydrogen concentration would be expected to control cladding hydride embrittlement and failure, rather than the average hydrogen concentration.

Finally, along with previous studies, it is crucial for researchers investigating hydride embrittlement during normal operation to design their experimental programs and analyses with careful consideration of hydride inhomogeneities.

## CRediT authorship contribution statement

**Katheren R.B. Nantes:** Conceptualization, Formal analysis, Methodology, Writing – original draft. **Miaomiao Jin:** Conceptualization, Formal analysis, Supervision, Writing – review & editing. **Arthur T. Motta:** Conceptualization, Formal analysis, Funding acquisition, Supervision, Writing – review & editing.

## Declaration of competing interest

The authors declare that they have no known competing financial interests or personal relationships that could have appeared to influence the work reported in this paper.

## Data availability

Data will be made available on request.

## Acknowledgements

This work was funded by the U.S. Department of Energy, as part of the Nuclear Energy University Program (DOE-NEUP) under grant # DE-NE0009130. This research made use of the resources of the High-Performance Computing Center at Idaho National Laboratory, which is supported by the Office of Nuclear Energy of the U.S. Department of Energy and the Nuclear Science User Facilities under Contract No. DE-AC07-05ID14517.

## Appendix A. Evaluation of the influence of a stress gradient on hydrogen diffusion

Once the hydrogen has entered the Zircaloy metal it can diffuse through the cladding, driven by concentration, temperature and stress gradients:

$$J_H = -D_H \nabla C_{ss} - D_H \frac{Q^* C_{ss} \nabla T}{RT^2} + D_H \frac{C_{ss} V}{RT} \nabla \sigma_H, \quad (A.1)$$

where  $C_{ss}$  is the amount of hydrogen in solid solution in wppm,  $R$  is the gas constant,  $T$  is the temperature,  $Q^*$  is the hydrogen heat of transport,  $V$  is the molar volume of hydrogen in Zr, and  $D_H$  is the hydrogen thermal diffusivity, calculated using the Arrhenius relation in Equation (A.2), in which  $1.08 \times 10^{-6}$  is the pre-exponential factor and  $4.4 \times 10^4$  is the hydrogen migration energy [46].

$$D_H [\text{m}^2/\text{s}] = 1.08 \times 10^{-6} \exp \left( -\frac{4.4 \times 10^4 \text{ J/mol}}{RT} \right). \quad (A.2)$$

To evaluate the influence of the stress gradient on diffusion compared to the influence of the concentration and temperature gradients, we consider only the radial dimension,  $D_H$  as a constant value throughout the clad thickness and estimated with the average temperature of 632 K,

$$D_H = 1.08 \times 10^{-6} \exp \left( -\frac{4.4 \times 10^4}{8.314 \times 632} \right) = 2.5 \times 10^{-10} \text{ m}^2/\text{s}. \quad (A.3)$$

We use the result of the output of our rodlet simulation, Subsection 3.1, at the inner cladding node there will be: 643 K, 109.7 wppm of  $C_{ss}$  and  $-2.5 \times 10^7$  Pa in normal stress in the radial direction. At the outer cladding node there will be: 622 K, 139.7 wppm and  $-1.7431 \times 10^7$  Pa. Assuming the heat of transport for hydrogen is 25,500 J/mol [47],  $V = 1.63 \text{ cm}^3/\text{mol}$ , as of [48], and the cladding has thickness of 575.3  $\mu\text{m}$  each term from Equation (A.1) will then become:

$$\begin{aligned} -D_H \nabla C_{ss} &= -2.5 \times 10^{-10} \times \frac{139.7 - 109.7}{575.3 \times 10^{-6}} \\ &= -1.3 \times 10^{-5} \text{ wppm} \times \text{m}^2/\text{s} \end{aligned} \quad (\text{A.4})$$

$$\begin{aligned} -D_H \frac{Q^* C_{ss} \nabla T}{RT^2} &= -2.5 \times 10^{-10} \times \frac{25500 C_{ss} \frac{622-643}{575.3 \times 10^{-6}}}{8.314 \times 632^2} \\ &= C_{ss} \times 7 \times 10^{-8} \text{ wppm} \times \text{m}^2/\text{s} \end{aligned} \quad (\text{A.5})$$

$$\begin{aligned} D_H \frac{C_{ss} V}{RT} \nabla \sigma_H &= -2.5 \times 10^{-10} \times \frac{C_{ss} 1.63 \times 10^{-6} (-1.7431 + 2.5) \times 10^7}{8.314 \times 632 \times 575.3 \times 10^{-6}} \\ &= C_{ss} \times 1.02 \times 10^{-9} \text{ wppm} \times \text{m}^2/\text{s} \end{aligned} \quad (\text{A.6})$$

As a result for this typical case, the stress gradient has an influence about 10 times lower than the temperature term and 10,000 times lower than the concentration gradient and thus may be neglected on the hydrogen flux calculation.

## Appendix B. BISON equations for hydride precipitation HNGD model

The BISON code uses the Hydride Nucleation-Growth-Dissolution (HNGD) model developed by [6–8,49] to calculate the hydrogen concentration and diffusion and hydrides precipitation. The change in hydrogen in solid solution with time is calculated by:

$$\frac{\partial C_{ss}}{\partial t} = -\nabla \left( -D_H \nabla C_{ss} - \frac{D_H Q^* C_{ss}}{RT^2} \nabla T \right) - S \quad (\text{B.1})$$

where,  $C_{ss}$  is the hydrogen in solid solution concentration,  $t$  is time,  $D_H$  is the hydrogen thermal diffusivity,  $Q^*$  is the hydrogen heat of transport,  $R$  is the gas constant,  $T$  is the temperature, and  $S$  is the hydride precipitation rate:

$$\frac{\partial C_{prec}}{\partial t} = S, \quad (\text{B.2})$$

which is given as a summation of the hydride nucleation rate ( $S_N$ ), growth rate ( $S_G$ ), and dissolution rate ( $S_D$ ). Those are calculated using the equations below,

$$S_N = \begin{cases} K_N (C_{ss} - TSS_P), & \text{if } C_{ss} > TSS_P \\ 0, & \text{else} \end{cases}, \quad (\text{B.3})$$

which describes the nucleation of hydrides that occurs once the concentration of hydrogen in solid solution is higher than the terminal solid solubility for precipitation ( $TSS_P$ ). The dissolution rate  $S_D$  is given by:

$$S_D = \begin{cases} K_D (C_{ss} - TSS_D), & \text{if } C_{ss} < TSS_D \text{ and } C_P > 0 \\ 0, & \text{else} \end{cases}. \quad (\text{B.4})$$

That is, hydride dissolution can occur when the concentration of hydrogen in solid solution is less than the terminal solid solubility for dissolution ( $TSS_D$ ) and there are hydrides present. In the hysteresis region ( $TSS_D < C_{ss} < TSS_P$ ) the hydride particles can grow according to,

$$S_G = \begin{cases} K_G (C_H - TSS_D) p (1-x) (-\ln(1-x))^{1-\frac{1}{p}}, & \text{if } C_{ss} > TSS_D \\ & \text{and } C_P > 0 \\ 0, & \text{else} \end{cases} \quad (\text{B.5})$$

where,  $K_N$ ,  $K_G$ , and  $K_D$  are the kinetics coefficients for nucleation, growth, and dissolution, respectively,  $C_{ss}$  is the concentration of hydrogen in solid solution,  $C_P$  is the concentration of hydrogen precipitated as hydride,  $C_H$  is the total hydrogen concentration,  $p$  represents the growth dimensionality (approximately 2.5 for platelets), and the degree of completion of the reaction  $x = \frac{C_H - C_{ss}}{C_H - TSS_D}$ .

The kinetic coefficients equations are summarized as:

$$K_N [s^{-1}] = 2.75 \times 10^{-5} (1 - v_\delta) \exp \left( -\frac{E_f(T)}{RT} \right) \quad (\text{B.6})$$

$$K_G [s^{-1}] = \left[ \frac{1}{5.35 \times 10^5 x_\alpha (1 - v_\delta) \exp \left( -\frac{E_g}{RT} \right)} + \frac{1}{1.6 \times 10^{-5} x_\alpha (1 - v_\delta) \exp \left( -\frac{E_f(T)}{RT} \right)} \right]^{-1} \quad (\text{B.7})$$

$$K_D [s^{-1}] = 1.11 \times 10^3 \exp \left( -\frac{E_D}{RT} \right), \quad (\text{B.8})$$

where,  $E_f(T)$  is the hydride formation energy,  $v_\delta$  is the hydride volume fraction,  $x_\alpha$  is the atomic fraction of hydrogen,  $E_g$  is the activation energy for growth by diffusion and equal to 86.8 kJ/mol [49], and  $E_D$  is the hydrogen diffusion activation energy and equal to  $4.4 \times 10^4$  J/mol [46].

## References

- [1] C. Lemaignan, A.T. Motta, Zirconium alloys in nuclear applications, *Mater. Sci. Technol. Compr. Treat.* 10B (1994) 1–51.
- [2] A.T. Motta, A. Couet, R.J. Comstock, Corrosion of zirconium alloys used for nuclear fuel cladding, *Annu. Rev. Mater. Res.* 45 (2015) 311–343.
- [3] A. Couet, A.T. Motta, A. Ambard, D. Livigni, In-situ electrochemical impedance spectroscopy measurements of zirconium alloy oxide conductivity: relationship to hydrogen pickup, *Corros. Sci.* 119 (2017) 1–13.
- [4] B. Kammenzind, D.G. Franklin, H.R. Peters, W.J. Duffin, Hydrogen pickup and redistribution in alpha-annealed Zircaloy-4, *ASTM Spec. Tech. Publ.* 1295 (1996) 338–369.
- [5] A.T. Motta, L. Capolungo, L.-Q. Chen, M.N. Cinbiz, M.R. Daymond, D.A. Koss, E. Lacroix, G. Pastore, P.-C.A. Simon, M.R. Tonks, et al., Hydrogen in zirconium alloys: a review, *J. Nucl. Mater.* 518 (2019) 440–460.
- [6] F. Passellaigue, E. Lacroix, G. Pastore, A.T. Motta, Implementation and validation of the hydride nucleation-growth-dissolution (HNGD) model in BISON, *J. Nucl. Mater.* 544 (2021) 152683.
- [7] F. Passellaigue, P.-C.A. Simon, A.T. Motta, Predicting the hydride rim by improving the solubility limits in the hydride nucleation-growth-dissolution (HNGD) model, *J. Nucl. Mater.* 558 (2022) 153363.
- [8] E. Lacroix, P.-C.A. Simon, A.T. Motta, J.D. Almer, Zirconium hydride precipitation and dissolution kinetics in zirconium alloys, *ASTM Spec. Tech. Publ.* 1597 (2021) 67–91.
- [9] R.L. Williamson, J. Hales, S. Novascone, M. Tonks, D. Gaston, C. Permann, D. Andrs, R. Martineau, Multidimensional multiphysics simulation of nuclear fuel behavior, *J. Nucl. Mater.* 423 (1–3) (2012) 149–163.
- [10] R. Asher, F. Trowse, The distribution of hydrogen in zirconium alloy fuel cladding: the effects of heat flux, *J. Nucl. Mater.* 35 (1) (1970) 115–121.
- [11] G. Marino, Hydrogen supercharging in Zircaloy, *Mater. Sci. Eng.* 7 (6) (1971) 335–341.
- [12] G. Marino, A numerical calculation of the redistribution of an interstitial solute in a thermal gradient, *Nucl. Sci. Eng.* 49 (1) (1972) 93–98.
- [13] A.D. Lindsay, D.R. Gaston, C.J. Permann, J.M. Miller, D. Andrš, A.E. Slaughter, F. Kong, J. Hansel, R.W. Carlsen, C. Icenhour, L. Harbour, G.L. Giudicelli, R.H. Stogner, P. German, J. Badger, S. Biswas, L. Chapuis, C. Green, J. Hales, T. Hu, W. Jiang, Y.S. Jung, C. Matthews, Y. Miao, A. Novak, J.W. Peterson, Z.M. Prince, A. Rovinelli, S. Schunert, D. Schwen, B.W. Spencer, S. Veeraraghavan, A. Recuero, D. Yushu, Y. Wang, A. Wilkins, C. Wong, 2.0 - MOOSE: enabling massively parallel multiphysics simulation, *SoftwareX* 20 (2022) 101202, <https://doi.org/10.1016/j.softx.2022.101202>, <https://www.sciencedirect.com/science/article/pii/S2352711022001200>.
- [14] J. Papin, B. Cazalis, J. Frizonnet, J. Desquines, F. Lemoine, V. Georgenthum, F. Lamare, M. Petit, Summary and interpretation of the CABRI REP-Na program, *Nucl. Technol.* 157 (3) (2007) 230–250.
- [15] G. Pastore, L. Luzzi, V. Di Marcello, P. Van Uffelen, Physics-based modelling of fission gas swelling and release in  $\text{UO}_2$  applied to integral fuel rod analysis, *Nucl. Eng. Des.* 256 (2013) 75–86.
- [16] D.L. Hargman, G.A. Reymann, MATPRO-Version 11: a handbook of materials properties for use in the analysis of light water reactor fuel rod behavior, *Tech. Rep. NUREG/CR-0497*, EG & G Idaho, 1979, <https://www.osti.gov/biblio/6442256>.

- [17] O. Diard, S. Leclercq, G. Rousselier, F. Azzouz, G. Cailletaud, Modeling of pellet-cladding interaction during power ramps in pressurized water reactors, Tech. Rep. Paper 1062, IASMiRT 16, 2001.
- [18] M.W. Heinstein, T.A. Laursen, An algorithm for the matrix-free solution of quasi-static frictional contact problems, *Int. J. Numer. Methods Eng.* 44 (9) (1999) 1205–1226.
- [19] I.G. Ritchie, Waterside corrosion of zirconium alloys in nuclear power plants, Tech. Rep. IAEA TECDOC 996, IAEA, 1998.
- [20] M. Limbäck, T. Andersson, A model for analysis of the effect of final annealing on the in- and out-of-reactor creep behavior of Zircaloy cladding, *ASTM Spec. Tech. Publ.* 1295 (1996) 448–468.
- [21] N. Hoppe, Engineering model for Zircaloy creep and growth, in: *International Topical Meeting on LWR Fuel Performance*, Avignon (France), 1991, pp. 157–172.
- [22] B. Spencer, D. Schwen, J. Hales, Multiphysics modeling of nuclear materials, in: *Handbook of Materials Modeling: Applications: Current and Emerging Materials*, 2020, pp. 2293–2312.
- [23] A.E. Slaughter, C.J. Permann, J.M. Miller, B.K. Alger, S.R. Novascone, Continuous integration, in-code documentation, and automation for nuclear quality assurance conformance, *Nucl. Technol.* 207 (7) (2021) 923–930, <https://doi.org/10.1080/00295450.2020.1826804>.
- [24] R.L. Williamson, C.P. Folsom, G. Pastore, S. Veeraraghavan, Reactivity insertion accident (RIA) capability status in the bison fuel performance code, Tech. Rep. INL/EXT-16-38861, Idaho National Lab. (INL), Idaho Falls, ID, United States, 2016.
- [25] V. Bobkov, L. Fokin, E. Petrov, V. Popov, V. Rumiantsev, A. Savvatimsky, Thermophysical properties of materials for nuclear engineering: a tutorial and collection of data, in: *IAEA-THPH*, 2008.
- [26] W.G. Luscher, K.J. Geelhood, Material property correlations: comparisons between FRAPCON-3.4, FRAPTRAN 1.4, and MATPRO, Tech. Rep. NUREG/CR-7024, Pacific Northwest National Lab. (PNNL), Richland, WA (United States), 2010.
- [27] K.J. Geelhood, W. Luscher, FRAPTRAN-1.5: Integral Assessment, Tech. Rep., vol. NUREG/CR-7023 Vol. 2, Rev.1, U.S. Nuclear Regulatory Commission, 2014.
- [28] J. Desquines, V. Georgenthum, F. Lemoine, B. Cazalis, The fracture and spallation of zirconia layers in high burnup PWR fuel claddings submitted to RIA transients, in: *Proceedings of 18th International Conference on Structural Mechanics in Reactor Technology (SMIRT)*, 2005, pp. 444–453.
- [29] A. Garde, G. Smith, R. Pirek, Effects of hydride precipitate localization and neutron fluence on the ductility of irradiated Zircaloy-4, *ASTM Int. STP* 1295 (1996) 407–430.
- [30] O. Pierron, D. Koss, A. Motta, R. Daum, K. Chan, Failure of Zircaloy-4 sheet containing hydride blisters, in: *Proceedings of the Nuclear Safety Research Conference*, Nuclear Regulatory Commission, 2002.
- [31] P. Clifford, Pressurized-water reactor control rod ejection and boiling-water reactor control rod drop accidents, Tech. Rep. RG 1.236, United States Nuclear Regulatory Commission, 2020.
- [32] R.S. Daum, S. Majumdar, H.C. Tsai, M.C. Billone, D.W. Bates, D.A. Koss, et al., On the embrittlement of Zircaloy-4 under RIA relevant conditions, *ASTM Spec. Tech. Publ.* 1423 (2002) 696–713.
- [33] R.S. Daum, A.T. Motta, Y. Chu, Identification and quantification of hydride phases in Zircaloy-4 cladding using synchrotron radiation diffraction, *J. Nucl. Mater.* 393 (3) (2009) 453–463.
- [34] M. Billone, T. Burtseva, R. Einziger, Ductile-to-brittle transition temperature for high-burnup cladding alloys exposed to simulated drying-storage conditions, *J. Nucl. Mater.* 433 (1–3) (2013) 431–448.
- [35] A.H. de Menibus, J. Sercombe, Q. Auzoux, C. Poussard, Thermomechanical loading applied on the cladding tube during the pellet cladding mechanical interaction phase of a rapid reactivity initiated accident, *J. Nucl. Mater.* 453 (1–3) (2014) 210–213.
- [36] O. Pierron, D. Koss, A. Motta, K. Chan, The influence of hydride blisters on the fracture of Zircaloy-4, *J. Nucl. Mater.* 322 (1) (2003) 21–35.
- [37] A. Glendenning, D. Koss, O. Pierron, A. Motta, R. Daum, Failure of hydrided Zircaloy-4 under equal-biaxial and plane-strain tensile deformation, *J. ASTM Int.* 2 (6) (2005) JAI12441.
- [38] D.D. Lanning, A. Johnson, D.J. Trimble, S. Boyd, Corrosion and hydriding of N reactor pressure tubes, *ASTM Int. STP* 1023 (1989) 3–19.
- [39] J. Zhang, Hydruration du Zircaloy-4 et étude de la distribution de l'hydrogène dans une gaine de combustible rep, Ph.D. thesis, Ecole Centrale de Paris, Châtenay-Malabry, 1992.
- [40] J. Zhang, M. Groos, T. Bredel, M. Trotabas, P. Combette, Quantification and characterization of zirconium hydrides in Zircaloy-4 by the image analysis method, *J. Nucl. Mater.* 195 (1/2) (1992) 17–23.
- [41] R. Montgomery, B.B. Bevard, R.N. Morris, J.S. Goddard Jr, S.K. Smith, J. Hu, J. Beale, B. Yoon, Sister rod nondestructive examination final report, Tech. Rep. ORNL/SPR-2018/801, Oak Ridge National Lab. (ORNL), Oak Ridge, TN (United States), 2018.
- [42] R.W. Shimskey, J.R. Allred, S.E. Asmussen, H.T. Brown, S.K. Cooley, R.C. Daniel, M.K. Edwards, J.G. Geeting, A. Goulet, C.H. Holbrook, et al., PNNL FY 2022 sibling pin testing results, Tech. Rep. PNNL-33781, Pacific Northwest National Laboratory (PNNL), Richland, WA (United States), 2023.
- [43] F. Schmitz, C. Gonnier, J. Papin, The status of the CABRI test program: Recent results and future activities, Tech. Rep. NUREG/CP-0157-VOL.1, US Nuclear Regulatory Commission (NRC), Washington, DC (United States), 1997.
- [44] F. Schmitz, J. Papin, High burnup effects on fuel behaviour under accident conditions: the tests CABRI REP-Na, *J. Nucl. Mater.* 270 (1–2) (1999) 55–64.
- [45] R. Montgomery, N. Waeckel, R. Yang, Topical report on reactivity initiated accidents: Bases for RIA fuel and core coolability, Tech. Rep. 1002865, Palo Alto, CA, 2002.
- [46] Y. Zhang, C. Jiang, X. Bai, Anisotropic hydrogen diffusion in  $\alpha$ -Zr and Zircaloy predicted by accelerated kinetic Monte Carlo simulations, *Sci. Rep.* 7 (2017) 1–13, <https://doi.org/10.1038/srep41033>.
- [47] S. Kang, P.-H. Huang, V. Petrov, A. Manera, T. Ahn, B. Kammenzind, A.T. Motta, Determination of the hydrogen heat of transport in Zircaloy-4, *J. Nucl. Mater.* 573 (2023) 154122.
- [48] R. Eadie, K. Tashiro, D. Harrington, M. Leger, The determination of the partial molar volume of hydrogen in zirconium in a simple stress gradient using comparative microcalorimetry, *Scr. Metall. Mater. (U.S.)* 26 (2) (1992).
- [49] E. Lacroix, Modeling zirconium hydride precipitation and dissolution in zirconium alloys, Ph.D. thesis, The Pennsylvania State University, 2019.